ACS Photonics

Letter

Cite This: ACS Photonics 2018, 5, 4776−4780

pubs.acs.org/journal/apchd5

Large Errors from Assuming Equivalent DC and High-Frequency Electrical Characteristics in Metal−Multiple-Insulator−Metal Diodes

Amina Belkadi, Ayendra Weerakkody, and Garret Moddel*

Department of Electrical, Computer and Energy Engineering, University of Colorado at Boulder, Boulder, Colorado 80309-0425, United States

Supporting Information

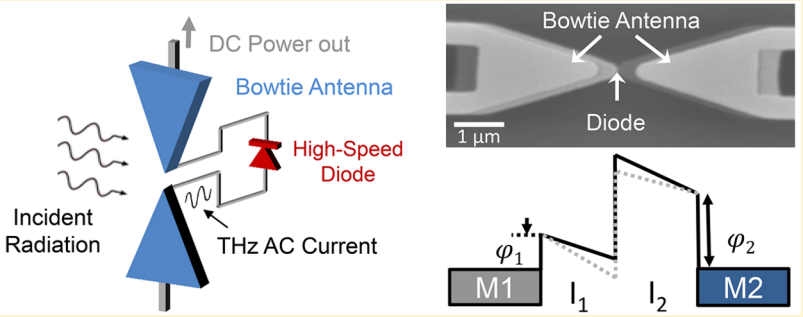

ABSTRACT: Metal−insulator−metal (MIM) tunnel diodes are essential for ultra-high-speed rectification. We review an erroneous method for distributing DC voltage drops across multiple insulator layers that is used in all the published literature on these devices. It has resulted in large errors between designed and fabricated multi-insulator diodes. For multi-insulator MIM diodes, voltage division is dependent on both tunneling resistances and oxide capacitances. We demonstrate that correct voltage division at DC is determined by the rectification resistance, as opposed to the commonly used capacitive voltage division. We find that DC characteristics of multi-insulator diodes cannot be used to predict high-frequency behavior.

KEYWORDS: *metal/insulator/metal (MIM) diode, optical rectenna, tunneling diodes, infrared, solar energy*

Metal−insulator−metal (MIM) tunnel diodes play an important role in many applications, such as energy harvesting,[1,2] infrared detection,[3−5] single-electron transistors,[6,7] resistive random access memory,[8,9] and matrix addressed displays.[10] For energy harvesting applications where MIM diodes operate as rectifiers, the diode capacitance (C) and resistance (R) determine the maximum operation frequency $f_c = 1/(2\pi RC)$. The ability to deposit ultrathin oxides and to combine multiple insulators in a device enables the tailoring of the diode's characteristics for high-frequency (THz) operation. Materials that have very low dielectric constants at terahertz frequencies, such as Al_2O_3,[11] can enhance nonlinearity as well as reduce diode capacitance. In a single-insulator MIM diode, Al_2O_3 forms a high barrier with most metals, thus increasing the diode resistance and lowering the cutoff frequency.[3,12−14] When combined with NiO, the overall diode DC resistance can be reduced,[15] but the challenge becomes optimizing the structure for high-frequency rectification. This requires accurate knowledge of the shape of the diode's energy band diagram, which changes with frequency. One method of assessing these diodes is to measure their high-frequency current−voltage $I(V)$ characteristics, which is a tedious and difficult process. The alternative is to develop simulation-based figures of merit that enable the use of material properties extracted from measured characteristics to compute the high-frequency $I(V)$ characteristics. This concept, that the $I(V)$ characteristics change with frequency, is commonly missed when designing multi-insulator diodes for terahertz operation, which leads to significant errors in assessing the potential of diodes for efficient energy harvesting. The main difficulty in designing multi-insulator diodes stems from correctly determining the slope of the conduction band edge of each dielectric, which is determined by the voltage division across each oxide.

By choosing different oxides with particular thicknesses and dielectric constant ratios, we can take advantage of voltage division across the insulators to enhance the diode's nonlinearity.[16] For a double insulator, as seen in Figures 1(a) and (b), the two oxides are in series, and each oxide can be represented with a simplified circuit diagram of a resistor and a capacitor in parallel. All MIM simulators described in the literature,[14,17−22] which are extensions of the Simmons tunneling model,[23] determine the voltage division across the insulators in DC based on dielectric constants and thicknesses. The flaw in this approach is that it does not take the tunneling resistance into account. This resistance, which depends on tunneling probability across oxides, governs voltage division at DC, where the capacitors are effectively open circuits, as depicted in Figure 1(c). At frequencies well above cutoff,

Received: October 8, 2018
Published: December 3, 2018

DOI: 10.1021/acsphotonics.8b01399
ACS Photonics 2018, 5, 4776−4780

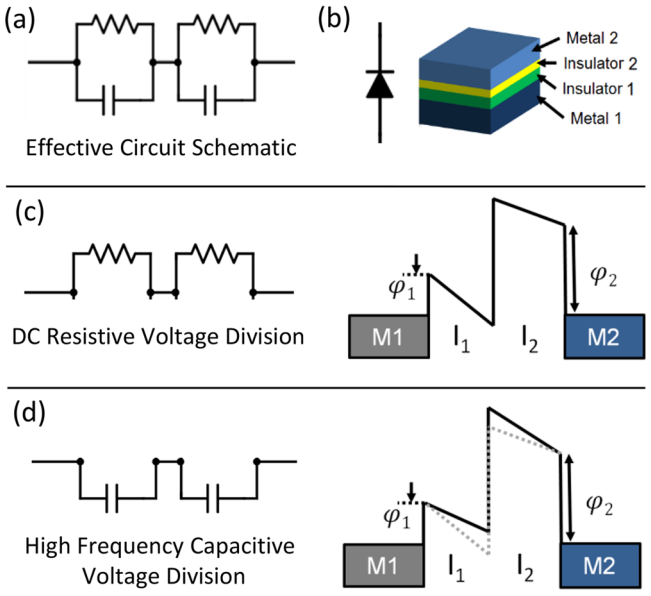

Figure 1. (a) Circuit diagram of a double-insulator MIM diode where each oxide is represented by a resistor and a capacitor in parallel. (b) MIM diodes are made of two very thin insulators (<5 nm) in series sandwiched between two metal contacts. (c) Resistive voltage division across insulators and band bending at DC. (d) Capacitive voltage division across insulators and band bending at high frequencies. The dotted line in the band diagram represents the DC bending due to resistive voltage division, for comparison.

where the magnitude of the capacitive reactances are smaller than the tunneling resistances, it is the capacitive voltage division that dominates, and therefore using a dielectric constant-based voltage division approach is valid, as depicted in Figure 1(d). This appears to be the reason that measured DC characteristics of double-insulator diodes do not match their simulated characteristics, and attempts to accurately design them have been unsuccessful. For the same reason, characteristics measured at DC have not correlated well with measured optical (AC) responses. Because of the incorrect voltage division at DC, the tunneling model will result in wrong fit parameters that will affect the predicted high-frequency $I(V)$ and the projected diode efficiency. We experimentally demonstrate and theoretically prove this concept by fabricating, measuring, and analyzing single- and double-insulator MIM diodes. We show that for double-insulator MIM diodes the change in voltage division between DC and high frequency is drastic and that using DC characteristics to predict high-frequency behavior leads to wrong conclusions.

RESULTS AND DISCUSSION

To determine the validity of resistive and capacitive voltage division among insulating layers, we use measurements and simulations to compare diode characteristics at DC and under 28 THz infrared illumination for single- and double-insulator diodes. We used a modified germanium shadow mask process[24] that facilitates a single self-aligned mask layer and enables the fabrication of structures with 100 nm feature sizes. The single-insulator MIM diode stack consists of 35 nm of thermally evaporated Ni, an effective thickness of 6 nm DC sputtered NiO, and 3 and 37 nm of evaporated Cr and Au, respectively. The double-insulator MIM diode stack consists of 37 nm of thermally evaporated Ni, an effective thicknesses of 3.5 and 0.73 nm of DC sputtered NiO and of RF sputtered Al_2O_3, respectively, followed by 3 nm of evaporated Cr and 62 nm of evaporated Au. The Ni/NiO interface was chosen for its low barrier height of approximately 0.1 eV,[25] which facilitates low-resistance devices. The Au layer was chosen for its low-loss tangent layer for optical measurements at 28 THz. To calculate the areas of the fabricated diodes, scanning electron microscopy (SEM) images were obtained (see the Supporting Information S1).

Following the fabrication of these diodes, we measured their DC $I(V)$ characteristics using a four-point probe setup to eliminate lead resistance effects of the probe/wiring structure. We swept the voltage over a limited range of −300 to +300 mV to avoid breaking down the sub-nanometer-thick dielectrics. The diode metrics of interest are the dynamic resistance ($R = 1/I'$) and responsivity ($\beta = [I''/(2I')]$) at zero applied voltage. Zero-bias values are sufficient to assess performance of these diodes in energy harvesting applications, where they self-bias at approximately 100 μV. The measured $I(V)$ data are fitted with an exponential fit[26] before extracting resistance and responsivity to eliminate measurement noise. Table 1 presents a summary of the DC zero-bias responsivity

Table 1. Responsivity and Resistance at Zero Applied Voltage for the Single-Insulator and Double-Insulator MIM Diodes

diode	β_0 (A/W)	R_0 (Ω)
Ni/NiO/CrAu	0.52	24.3 k
Ni/NiO/Al_2O_3/CrAu	0.38	13.8 k

(β_0) and zero-bias resistance (R_0) values for the fabricated single- and double-insulator MIM structures (see the Supporting Information S2 and S3 for diode $I(V)$ curves and voltage-dependent responsivity and resistance plots).

To assess the mid-infrared response of the fabricated rectenna system, both open-circuit voltage (V_{oc}) and short-circuit current (I_{sc}) were measured under 10.6 μm illumination. The rectenna consists of a bow-tie antenna with two opposing triangular sections and a diode junction at its feed point. The measurements were performed using a linearly polarized pulsed CO_2 laser having a maximum beam intensity of 1 W/mm^2. Since the area of the rectenna is 24 μm^2, this corresponds to an input power (P_{in}) of 24 μW. Based on a clamping circuit model of the rectenna configuration[1] and the fact that the $I(V)$ curve is linear in the low voltages range, the ratio of V_{oc} and I_{sc} is a measure of the high-frequency diode resistance (R_0^{HF}), with the values summarized in Table 2.

Table 2. Measured Optical Response Values for the Diodes at 10.6 μm

diode	V_{oc} (μV)	I_{sc} (nA)	R_0^{HF} (Ω)	R_0^{DC} (Ω)	ΔR_0 (%)
Ni/NiO/CrAu	11.2	0.42	27 k	24.3 k	11
Ni/NiO/Al_2O_3/CrAu	53.2	2.17	24.5 k	13.8 k	86

The best indication of a change in voltage division is the comparison between DC and high-frequency resistances for our fabricated diodes. Because there is no change in distribution of voltage for a single-insulator MIM diode, there should be no changes in the measured zero-bias resistance between DC and high frequencies. Small variations

DOI: 10.1021/acsphotonics.8b01399
ACS Photonics 2018, 5, 4776−4780

are expected due to lead resistance from two-point probe optical measurements and laser instabilities due to beam wander. For a double-insulator structure, the change in voltage division from resistive to capacitive across the insulators alters the band bending and affects tunneling characteristics of the diode at high frequencies, thus producing completely different $I(V)$ characteristics. To confirm this, we compare measured high-frequency diode resistance (R_0^{HF}) to DC resistance (R_0^{DC}) by computing a percentage change (ΔR_0). The 11% change in R_0^{HF} of the single-insulator MIM is attributed to a measured lead resistance of 600 Ω and a laser beam instability margin of error (<10%). The 86% increase in R_0^{HF} for the double-insulator MIM structure can be explained by neither pure lead resistance nor the laser instability margin of error. The only possible explanation for the increase in resistance is the change in voltage division across insulators, where more voltage is applied on Al_2O_3. In the following section, we investigate this theoretically by simulating the measured DC $I(V)$ characteristics using a resistive voltage division approach and fitting the high-frequency $I(V)$ characteristics by a capacitive voltage division approach.

The complexity of modeling and analyzing multi-insulator MIM diodes increases with the number of oxides used. For a single-insulator MIM, the process is simple, and an accurate fit between simulated and measured data can be achieved[13,15,22,27,28] since there are only three main parameters to change: the barrier heights, the thickness of the oxide, and the effective mass of electrons. As the number of insulators increases, the number of fit parameters increases linearly and voltage division across the insulators becomes a concern, thus increasing the difficultly of achieving an accurate fit.[18,20,21] To correctly fit our double-insulator diodes, we started by extracting as much information as possible about the structure: the thickness of both oxides using variable-angle spectroscopic ellipsometry (VASE) and the Ni/NiO interface by building a single-insulator diode. We expect the oxide in our simulations to be thinner than the measured values because of surface nonuniformity across the diode junction and the fact that tunneling probability increases in thin regions over thick ones, thus dominating the diode $I(V)$ characteristics. Figure 2 presents a good correspondence between our measured and simulated single-insulator diode. We determined a Ni/NiO barrier height of 0.12 eV. This leaves the second barrier height and the voltage division across the insulators as parameters to vary for the double-insulator diode (see the Supporting Information S3). Figure 3 presents simulation results that accurately fit measured data for a double-insulator diode. The resistive voltage division ends up being 83% across NiO and 17% across Al_2O_3. For DC, this is the voltage division that maximizes the current across the insulators. If material properties such as barrier heights and oxide thicknesses could be accurately determined for a stack, the simulator can then be used as a design tool to simulate DC $I(V)$ characteristics with voltage ratios that maximize the current though oxides.

The high-frequency $I(V)$ characteristic of the diode is generated using the material parameters determined from the DC fit of the diode (see the Supporting Information S3), with a change to capacitive dielectric-dependent voltage division, as seen in Figure 4. We implement a quantum-mechanical image force lowering theory and find that the effects are negligible at 28 THz.[29] The effective mass of electrons is also varied since it

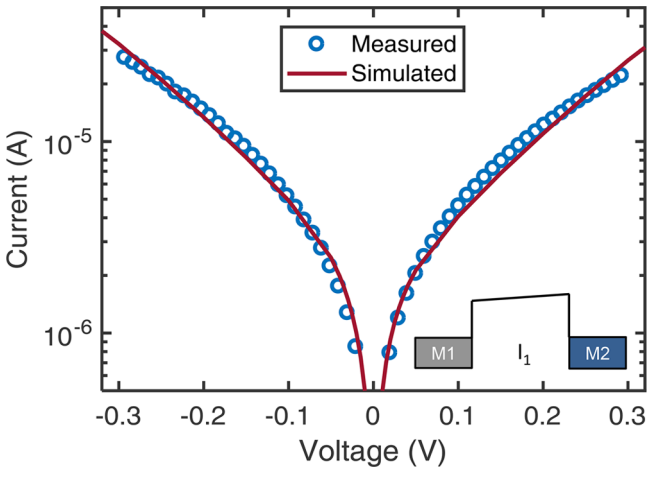

Figure 2. Diode simulation of the single-insulator diode at DC to extract diode oxide thickness for dielectric constant estimation and Ni/NiO barrier information for the double-insulator diode analysis.

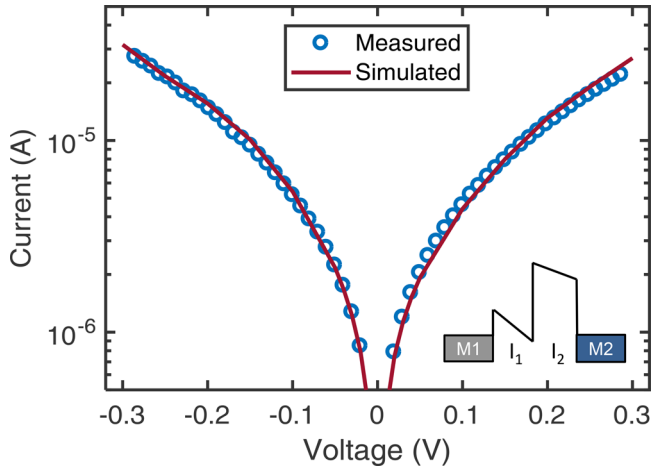

Figure 3. Diode simulation of the double-insulator diode at DC to predict high-frequency $I(V)$ characteristic.

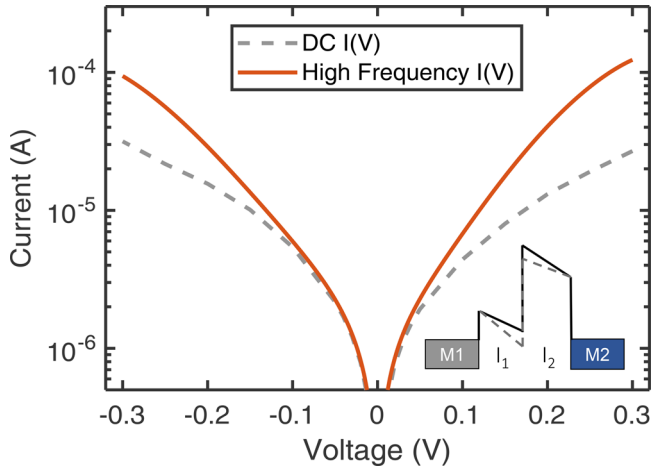

Figure 4. DC and high-frequency $I(V)$ characteristics of the double-insulator MIM diode. The inset represents the band diagram of the structure with both resistive (dashed gray) and capacitive (solid orange) voltage divisions.

DOI: 10.1021/acsphotonics.8b01399
ACS Photonics 2018, 5, 4776−4780

is frequency dependent. This is done simultaneously with the waterfall diagram analysis (see the Supporting Information S7), which uses the high-frequency zero-bias resistance, zero-bias responsivity, and the dielectric constants to calculate a projected open-circuit voltage and short-circuit current. The estimated dielectric constants from our high-frequency fit for NiO and Al_2O_3 were 7 and 3.85, respectively. These dielectric constant values are currently fit parameters that contain numerous frequency-dependent parameters not considered in the analysis. The capacitive voltage division results in 73% across NiO and 27% with a high-frequency resistance of 25.6 kΩ (see the Supporting Information S5 and S6). The measured high-frequency resistance of 24.5 kΩ is well within the 11% error margin. The close correspondence between the measured and simulated high-frequency resistance values confirms the change in voltage division from resistive to capacitive at high frequencies. It is also confirmation that DC diode characteristics cannot be used to predict high-frequency $I(V)$ characteristics. For our fabricated diodes, this is evident from the efficiency calculations of both diodes (see the Supporting Information S7), where the double-insulator diode's measured efficiency is approximately 23 times larger than that of the single insulator, whereas based on the DC characteristics, the single-insulator efficiency would surpass the double-insulator's by a factor of 1.2. For our double-insulator MIM diode with a cutoff frequency of 31 GHz, the tunneling resistance of the diode is 900 times larger than the capacitive reactance at 28 THz, which allows us to use a purely capacitive voltage division at this frequency. A combination of resistive and capacitive voltage division becomes necessary at frequencies below the cutoff frequency, which is theoretically difficult to determine.

CONCLUSIONS

In analyzing double-insulator MIM diodes, the correct method of dividing the voltage across the two insulator layers in DC is through resistive voltage division, where each oxide is modeled by a resistance. The simulated oxide resistances are fictitious elements used to achieve resistive voltage division for tunneling simulations. At frequencies higher than the RC cutoff, the commonly used dielectric-dependent capacitive voltage division method still applies. While a single-insulator diode $I(V)$ curve remains almost the same at DC and high frequencies, we experimentally demonstrate that the $I(V)$ characteristic of a double-insulator diode can change dramatically. The change is evident in the zero-bias resistance of a double-insulator diode changing by 86% between DC and high frequency as opposed to the 11% change for the single-insulator diode. The erroneous assumption that the DC and high-frequency $I(V)$ characteristics are the same has led to incorrect projections of device operating properties at high frequency and puzzling DC $I(V)$ curves that cannot be reconciled with designs based on simulations that assume capacitive voltage division.

METHODS

Fabrication. A modified germanium shadow mask process[24] was used that facilitates a single, self-aligned mask layer to be used to fabricate MIM diode structures with 100 nm feature sizes. The cross-section (Supporting Information S8) shows the suspended germanium bridge supported by unetched poly(methyl methacrylate) (PMMA) out of plane of the cross-section. The first step of the process was to spin coat ∼280 nm PMMA on a highly resistive p-type Si substrate coated with thermally grown 300 nm SiO_2. Next, 60 nm of germanium was evaporated on PMMA. The pattern was printed on the surface of the wafer by an ASML 5500 248 nm DUV stepper. Afterward the pattern was transferred into germanium with a CF_4 reactive ion etch followed by a O_2 plasma etch to remove the underlayer of PMMA. The O_2 plasma was run at a relatively high pressure of 600−800 mTorr to achieve an undercut of at least 250 nm under the germanium. Bridge widths less than 500 nm were obtained. The main limitation of this process is the requirement of angled metal depositions to achieve the necessary overlap, which limits which materials may be deposited.

Experimental Setup. The rectenna was illuminated with 10.6 μm linearly polarized radiation from a pulsed Synrad 48-1SWJ CO_2 laser. This was pulse width modulated by an Agilent 33220A function generator at 20 kHz. To monitor the noise level under dark conditions, the laser beam is passed through a ThorLabs SH05 shutter. A half-wave plate (ThorLabs PRM1Z8) was used in the optical path to rotate the laser polarization with respect to the antenna axis. The reference to the lock-in amplifier (SR830) was generated by a mechanical chopper at 1.7 kHz (see the Supporting Information S9).

ASSOCIATED CONTENT

Supporting Information

The Supporting Information is available free of charge on the ACS Publications website at DOI: 10.1021/acsphotonics.8b01399.

Additional information on characterization of the single-insulator and double-insulator diodes, including diode areas from SEM images, exponential fitting parameters, tunneling simulation parameters, efficiency and detectivity calculation, and germanium shadow mask process along with optical setup (PDF)

AUTHOR INFORMATION

Corresponding Author

*E-mail: moddel@colorado.edu.

ORCID

Amina Belkadi: 0000-0001-6575-5197

Garret Moddel: 0000-0002-1397-0319

Notes

The authors declare the following competing financial interest(s): G. Moddel holds stock in RedWave Energy, Inc.

ACKNOWLEDGMENTS

The authors would like to thank David Doroski for assistance with fabrication of the structures, John Stearns for valuable discussions and helpful comments, and Brad Pelz for the idea of DC voltage division determination through current maximization. This work was carried out in part under contract from RedWave Energy Inc. and funded in part by the Advanced Research Projects Agency−Energy (ARPA-E), U.S. Department of Energy, under Award Number DE-AR0000676. A portion of the fabrication was carried out at UCSB Nanofabrication Facility.

DOI: 10.1021/acsphotonics.8b01399
ACS Photonics 2018, 5, 4776−4780

REFERENCES

(1) Moddel, G.; Grover, S. *Rectenna Solar Cells*; Springer, 2013; Vol. 4.

(2) Briones, E.; Alda, J.; González, F. J. Conversion efficiency of broad-band rectennas for solar energy harvesting applications. *Opt. Express* **2013**, *21*, A412−A418.

(3) Bean, J. A.; Weeks, A.; Boreman, G. D. Performance Optimization of Antenna-Coupled Al AlO Pt Tunnel Diode Infrared Detectors. *IEEE J. Quantum Electron.* **2011**, *47*, 126−135.

(4) Dees, J. Detection and harmonic generation in the submillimeter wavelength region(Harmonic generation and detection in submillimeter wavelength region, emphasizing crystal point contact diode). *Microwave J.* **1966**, *9*, 48−55.

(5) Fumeaux, C.; Herrmann, W.; Kneubühl, F.; Rothuizen, H. Nanometer thin-film Ni−NiO−Ni diodes for detection and mixing of 30 THz radiation. *Infrared Phys. Technol.* **1998**, *39*, 123−183.

(6) Karbasian, G.; McConnell, M. S.; George, H.; Schneider, L. C.; Filmer, M. J.; Orlov, A. O.; Nazarov, A. N.; Snider, G. L. Metalinsulator-metal single electron transistors with tunnel barriers prepared by atomic layer deposition. *Appl. Sci.* **2017**, *7*, 246.

(7) Matsumoto, K. Room temperature operated single electron transistor made by STM/AFM nano-oxidation process. *Phys. B* **1996**, *227*, 92−94.

(8) Niu, G.; Kim, H.-D.; Roelofs, R.; Perez, E.; Schubert, M. A.; Zaumseil, P.; Costina, I.; Wenger, C. Material insights of HfO 2-based integrated 1-transistor1-resistor resistive random access memory devices processed by batch atomic layer deposition. *Sci. Rep.* **2016**, *6*, 28155.

(9) Vallée, C.; Gonon, P.; Jorel, C.; El Kamel, F.; Mougenot, M.; Jousseaume, V. High κ for MIM and RRAM applications: Impact of the metallic electrode and oxygen vacancies. *Microelectron. Eng.* **2009**, *86*, 1774−1776.

(10) Tannas, L. E. Evolution of flat-panel displays. *Proc. IEEE* **1994**, *82*, 499−509.

(11) Kischkat, J.; Peters, S.; Gruska, B.; Semtsiv, M.; Chashnikova, M.; Klinkmüller, M.; Fedosenko, O.; Machulik, S.; Aleksandrova, A.; Monastyrskyi, G.; Flores, Y. Midinfrared optical properties of thin films of aluminum oxide, titanium dioxide, silicon dioxide, aluminum nitride, and silicon nitride. *Appl. Opt.* **2012**, *51*, 6789−6798.

(12) Weerakkody, A.; Sedghi, N.; Mitrovic, I.; Van Zalinge, H.; Noureddine, I. N.; Hall, S.; Wrench, J.; Chalker, P.; Phillips, L.; Treharne, R.; Durose, K. Enhanced low voltage nonlinearity in resonant tunneling metal−insulator−insulator− metal nanostructures. *Microelectron. Eng.* **2015**, *147*, 298−301.

(13) Jayaswal, G.; Belkadi, A.; Meredov, A.; Pelz, B.; Moddel, G.; Shamim, A. Optical rectification through an Al 2 O 3 based MIM passive rectenna at 28.3 THz. *Materials Today Energy* **2018**, *7*, 1−9.

(14) Mitrovic, I.; Weerakkody, A.; Sedghi, N.; Ralph, J.; Hall, S.; Dhanak, V.; Luo, Z.; Beeby, S. Controlled modification of resonant tunneling in metal-insulator-insulator-metal structures. *Appl. Phys. Lett.* **2018**, *112*, No. 012902.

(15) Weerakkody, A.; Belkadi, A.; Moddel, G. Towards a practical Al_2O_3-based metalinsulator-metal infrared rectenna. *To be Submitted.*

(16) Grover, S.; Moddel, G. Metal single insulator and multi-insulator diodes for rectenna solar cells. In *Rectenna Solar Cells*; Springer, 2013; pp 89−109.

(17) Grover, S.; Moddel, G. Engineering the current−voltage characteristics of metal− insulator−metal diodes using double-insulator tunnel barriers. *Solid-State Electron.* **2012**, *67*, 94−99.

(18) Hashem, I. E.; Rafat, N. H.; Soliman, E. A. Theoretical study of metalinsulator-metal tunneling diode figures of merit. *IEEE J. Quantum Electron.* **2013**, *49*, 72−79.

(19) Hegyi, B.; Csurgay, A.; Porod, W. Investigation of the nonlinearity properties of the DC IV characteristics of metal-insulatormetal (MIM) tunnel diodes with doublelayer insulators. *J. Comput. Electron.* **2007**, *6*, 159−162.

(20) Herner, S.; Weerakkody, A.; Belkadi, A.; Moddel, G. High performance MIIM diode based on cobalt oxide/titanium oxide. *Appl. Phys. Lett.* **2017**, *110*, 223901.

(21) Herner, S. B.; Belkadi, A.; Weerakkody, A.; Pelz, B.; Moddel, G. Responsivity-resistance relationship in MIIM diodes. *J. Photovoltaics* **2017**.

(22) Abdolkader, T. M.; Shaker, A.; Alahmadi, A. Numerical simulation of tunneling through arbitrary potential barriers applied on MIM and MIIM rectenna diodes. *Eur. J. Phys.* **2018**, *39*, No. e045402.

(23) Simmons, J. G. Generalized formula for the electric tunnel effect between similar electrodes separated by a thin insulating film. *J. Appl. Phys.* **1963**, *34*, 1793−1803.

(24) Pelz, B.; Moddel, G. Distributed capacitance compensation in a metal-insulatormetal infrared rectenna using a traveling wave diode at 10.6 μm. *To be submitted.*

(25) Hobbs, P. C.; Laibowitz, R. B.; Libsch, F. R. Ni−NiO−Ni tunnel junctions for terahertz and infrared detection. *Appl. Opt.* **2005**, *44*, 6813−6822.

(26) Pelz, B.; Belkadi, A.; Moddel, G. Avoiding erroneous analysis of MIM diode current-voltage characteristics through exponential fitting. *Measurement* **2018**, *120*, 28−33.

(27) Eliasson, B. J. Metal-insulator-metal diodes for solar energy conversion. Ph.D. thesis, University of Colorado, 2001.

(28) Joshi, S. Performance limits of optical rectennas. Ph.D. thesis, University of Colorado at Boulder, 2015.

(29) Hartstein, A.; Weinberg, Z.; DiMaria, D. Experimental test of the quantummechanical image-force theory. *Phys. Rev. B: Condens. Matter Mater. Phys.* **1982**, *25*, 7174.

DOI: 10.1021/acsphotonics.8b01399
ACS Photonics 2018, 5, 4776−4780